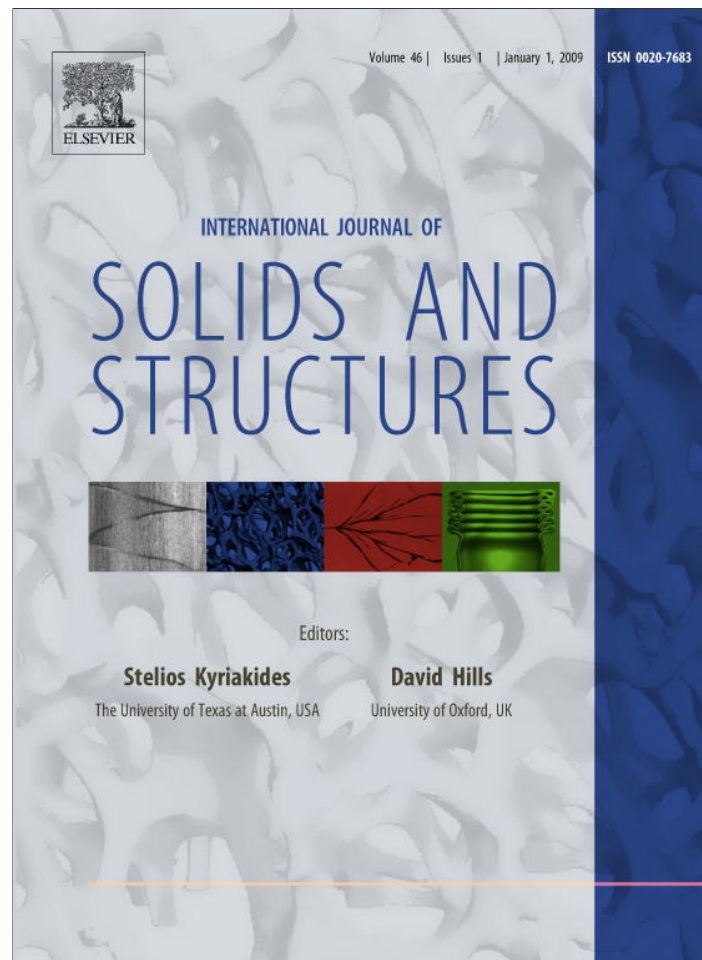


Provided for non-commercial research and education use.
Not for reproduction, distribution or commercial use.



This article appeared in a journal published by Elsevier. The attached copy is furnished to the author for internal non-commercial research and education use, including for instruction at the authors institution and sharing with colleagues.

Other uses, including reproduction and distribution, or selling or licensing copies, or posting to personal, institutional or third party websites are prohibited.

In most cases authors are permitted to post their version of the article (e.g. in Word or Tex form) to their personal website or institutional repository. Authors requiring further information regarding Elsevier's archiving and manuscript policies are encouraged to visit:

<http://www.elsevier.com/copyright>



Contents lists available at ScienceDirect

International Journal of Solids and Structures

journal homepage: www.elsevier.com/locate/ijsolstr

Direct extraction of rate-dependent traction–separation laws for polyurea/steel interfaces

Yong Zhu^a, Kenneth M. Liechti^{b,*}, K. Ravi-Chandar^b

^a Department of Mechanical and Aerospace Engineering, North Carolina State University, Raleigh, NC 27695, USA

^b Research Center for the Mechanics of Solids, Structures and Materials, Aerospace Engineering and Engineering Mechanics, The University of Texas, Austin, TX 78712, USA

ARTICLE INFO

Article history:

Received 19 November 2007
Received in revised form 12 July 2008
Available online 28 August 2008

Keywords:

Polyurea
Adhesion
Interfacial fracture
Cohesive zone model
Traction–separation law

ABSTRACT

Polyurea coatings on steel form tough, flexible and chemically resistant surfaces, making them ideal for a variety of applications. An important issue for polyurea coatings in some cases is their adhesion to steel under various loading conditions in aggressive environments. In this paper, adhesion was examined using steel/polyurea/steel sandwich specimens and interfacial fracture mechanics. The mode 1 and mode 2 interfacial fracture behaviors were characterized by two independent traction–separation laws. The traction–separation laws were measured directly by recording the J -integral and the end-opening displacement in the directions normal and tangential to the steel/polyurea interface. In each case, the traction was initially nonzero, increased with increasing separation, reached its peak value and then decreased with further increasing opening. Strong rate-dependent effects were found for both modes of fracture and were attributed to the interfacial behavior. Porosity introduced during the processing of the polyurea affected the traction–separation laws and associated fracture mechanisms.

© 2008 Elsevier Ltd. All rights reserved.

1. Introduction

Polyurea-based coatings are usually two-component systems that are made up of an isocyanate and a resin blend consisting of only amine terminated components. Polyurea coatings offer unique advantages in both manufacturing (they can be sprayed on and cure rapidly even at freezing temperatures) and properties (high deformability, high abrasive resistance, insensitivity to solvents, and low or zero volatile organic compounds) (Takas, 2004). These features are superior to most, if not all the other coatings currently available, which has allowed polyurea coatings to grow rapidly in a variety of applications. A critical issue for the reliability of polyurea coatings is their adhesion to substrates. However, to the best of our knowledge, very little, if any, data have been obtained for the adhesion of polyurea coatings, particularly in the form of traction–separation laws.

A practical approach for characterizing the adhesion of polymer coatings to metal substrates is to use sandwich specimens, which can be analyzed using interfacial linear elastic fracture mechanics (LEFM) concepts (Hutchinson and Suo, 1992). However, there can be limitations to the use of LEFM in sandwich structures. The first is that the assumed stress fields are not rigorously correct, for example, in the case of large-scale plasticity or in the case of very thin layers where the K -dominant field cannot develop (Wang, 1983). The second is that some joints may not have macroscopic defects large enough to be considered cracks for the purpose of fracture mechanics (Li et al., 2005b). These issues can compromise the utility of LEFM and alternative approaches must be sought. Cohesive zone modeling is one such approach. The key concept of cohesive zone

* Corresponding author. Fax: +1 512 471 5500.

E-mail address: kml@mail.utexas.edu (K.M. Liechti).

modeling is that the failure process zone can be described by a traction–separation law; more specifically, the cohesive traction, $\sigma(\delta)$, can vary along the failure process zone, but only depends on the local opening, δ .

Cohesive zone models are built upon the concepts first discussed by Dugdale (1960) and Barenblatt (1962). The key is the introduction of a second fracture parameter, e.g., the cohesive strength, in addition to the fracture toughness. This cohesive strength relates the toughness to the critical crack-tip opening required for crack propagation. Recently cohesive zone modeling has been applied to solve interfacial fracture problems. Needleman (1987) and Needleman (1990) proposed a cohesive zone model for analyzing void nucleation, growth and coalescence. In this model, the plane of the crack is held by a spring-like entity possessing a built-in traction–separation law. Extension of this model to analyzing interface debonding under mixed-mode conditions was provided by Tvergaard and Hutchinson (1993, 1994). In their analyses, fracture occurs when the normal and the tangential displacement at the tip of the cohesive zone fulfill a critical vectorial crack opening displacement (Liechti and Knauss, 1982). More recently, Yang and Thouless (2001) proposed a modified criterion for mixed-mode interfacial fracture, in which fracture occurs when the mode 1 and mode 2 energy release rates for the cohesive zone reach a critical value. Nevertheless, in both criteria, with independently characterized mode 1 and mode 2 traction–separation laws available, mixed-mode problems with a range of fracture mode-mixes can be fully solved.

Cohesive zone modeling has been used to examine a wide spectrum of interface problems, such as glass/epoxy interfacial fracture and adhesion (Swadener and Liechti, 1998), delamination in stitched composites (Massabo et al., 1998), plastic dissipation in thin debonding films (Shirani and Liechti, 1998), crack nucleation at bi-material corners (Mohammed and Liechti, 2000) and peeling (Kim and Aravas, 1988; Yang et al., 2000; Kinloch et al., 1994; Wei and Hutchinson, 1998). However, these models did not consider rate dependence in interface properties. Recently, rate-dependent traction–separation laws were measured for quasi-static debonding at polyurethane/steel (Sorensen, 2002) and rubber/steel (Liechti and Wu, 2001) interfaces. In addition, rate-dependent traction–separation laws have been determined for homogeneous polymeric materials (Ivankovic et al., 2004; Landis et al., 2000) considering the time-dependence of the damage growth processes and the non-linear viscoelastic response of ligaments in the fracture process zone.

Most approaches for measuring traction–separation laws rely on iterative comparisons between measured properties [e.g., an *R*-curve (Flinn et al., 1993), a crack opening profile (Cox and Marshall, 1991; Mello and Liechti, 2006) or a load–displacement curve (Li et al., 2005a)] with predictions based on assumed traction–separation laws. Two methods that yield the traction–separation law directly from experiments without such comparison are available. One is through direct tension or shear experiments (Cotterell and Mai, 1996; Pandya and Williams, 2000). However, in these experiments, the damage evolution across the width of the specimen must be uniform, which is usually difficult to achieve. In the second approach, the cohesive law is derived from simultaneous measurements of the *J*-integral and the end-opening (both normal and shear) of the cohesive zone. This has been successfully employed in the extraction of traction–separation laws for cementitious components (Li et al., 1987), adhesive bonds (Sorensen, 2002) and fiber-reinforced composites (Sorensen and Jacobsen, 2003). Both direct methods will be employed in the present work, although the focus is on the second one.

The main objective of the present paper is to obtain the traction–separation laws of a polyurea/steel interface in mode 1 and mode 2 directly from experiments using sandwich specimens. We begin by describing the experimental methods that were used for characterizing the mechanical behavior of polyurea and fracture at polyurea/steel interfaces. Next, we report on the tensile and shear behaviors of bulk polyurea prior to the experimental identification of mode 1 and mode 2 traction–separation laws for polyurea/steel interfaces at different loading rates. The paper closes with a discussion of the rate dependence of polyurea/steel interfaces and the effects of the manufacturing process on the interfacial failure mechanisms.

2. Experimental

The uniaxial tension and shear properties of bulk polyurea were measured in unconfined and sandwich configurations. The latter were also used in the fracture experiments in modes 1 and 2 for determining the traction–separation laws for the polyurea/steel interface. In this section, specimens and experimental procedures for all these experiments are described.

2.1. Specimen preparation

The specimens for measuring the unconfined tensile behavior of the polyurea were obtained from thin films. In this case, the polyurea fluid was sprayed on top of a Teflon block to form a thin film with thickness of 0.7 ± 0.1 mm. After the film was peeled from the Teflon block, tensile coupons were cut from the film using a stamp that produced the geometry shown in Fig. 1(a) with $l = 50.4$ mm and $w = 2.1$ mm.

The specimens for unconfined shear testing of the polyurea were cut from a thick block. The polyurea block was sprayed in a mold with Teflon bottom and sidewalls. The butterfly-shaped specimens were loaded using the Arcan apparatus (Popelar and Liechti, 1997; Arcan et al., 1978), as shown in Fig. 1(b). The gauge length l , width w and thickness B of the specimens were 16.1, 10.2, and 2.5 mm, respectively.

Steel/polyurea/steel sandwiches were used for examining the confined stress–strain response in tension and shear and determining the mode 1 and 2 traction–separation laws. The specimens were processed as follows: cold rolled steel adherends (Westbrook Metals, Austin, TX) were sandblasted and degreased with acetone prior to spraying. The polyurea formulation was developed by Texas Research International, Inc. (Austin, TX). The polyurea fluid, coming from two separate

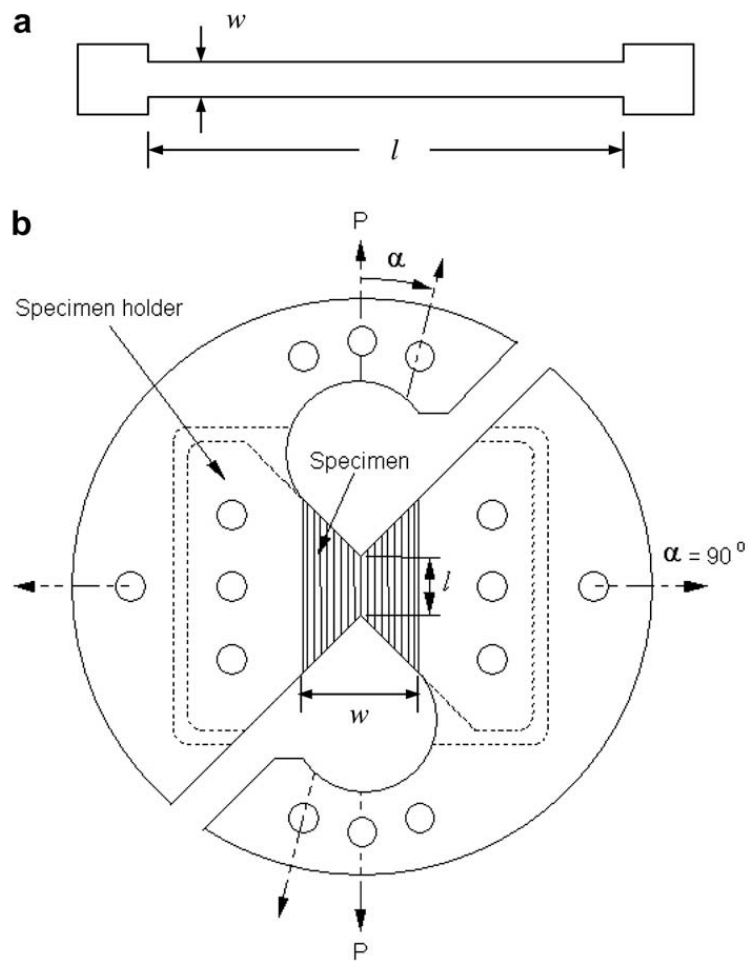


Fig. 1. (a) Tensile coupon for bulk polyurea, with a length of 50.8 mm, a width of 2.1 mm and a thickness of 0.7 mm. (b) Butterfly-shaped shear specimens for bulk polyurea, with a gauge length of 16.1 mm, a width of 10.2 mm and a thickness of 2.5 mm loaded in an Arcan apparatus.

reservoirs of resin and hardener, were combined in a single jet and sprayed on top of two steel plates that were 150 mm square by 4.76 mm thick. Immediately after the spraying was completed, the plates were joined and held together by four strong clamps at the corners. This process had to be accomplished within 10 s, the approximate reaction time. The adhesive thickness was basically controlled by the clamp pressure which gave rise to a uniform polyurea thickness of 0.7 ± 0.05 mm throughout the entire sandwich. The sandwich plates were left for at least 10 days for hardening at room temperature in an ambient environment before being subsequently machined into specimens.

2.2. Test methods

The test method for the uniaxial tension experiments was quite standard. Details of the apparatus and experimental procedures for Arcan testing in unconfined shear using the butterfly specimens have been given elsewhere (Popelar and Liechti, 1997; Arcan et al., 1978).

The double cantilever beam (DCB) configuration was used to determine the mode I traction–separation laws. The specimen geometry and the loading are shown in Fig. 2(a). A preexisting crack in the middle of the polyurea layer was cut using a sharp razor blade. It turned out that the fracture process zone in these experiments was large (Parmigiani and Thouless, 2007). Consequently, it was necessary to include (Högberg et al., 2007) the contribution of the rotation near the crack front to the J -integral through

$$J = 12 \frac{(pa)^2}{Eh^3} + P(w'_1 - w'_2). \quad (1)$$

where P is the applied load per unit width, a is the crack length, h is the adherend thickness, and E is the elastic modulus of the steel adherends, and w'_1 and w'_2 are, respectively, the rotations of the upper and lower adherends at the crack tip.

The J -integral approach can be applied if the materials possess an elastic stress–strain behavior. This was the case for steel adherends which were loaded below their yield strength (~ 500 MPa). The polyurea is an elastomer, which was considered to be a nonlinear elastic material. Evaluating J -integral along a path just outside of the failure process zone yields

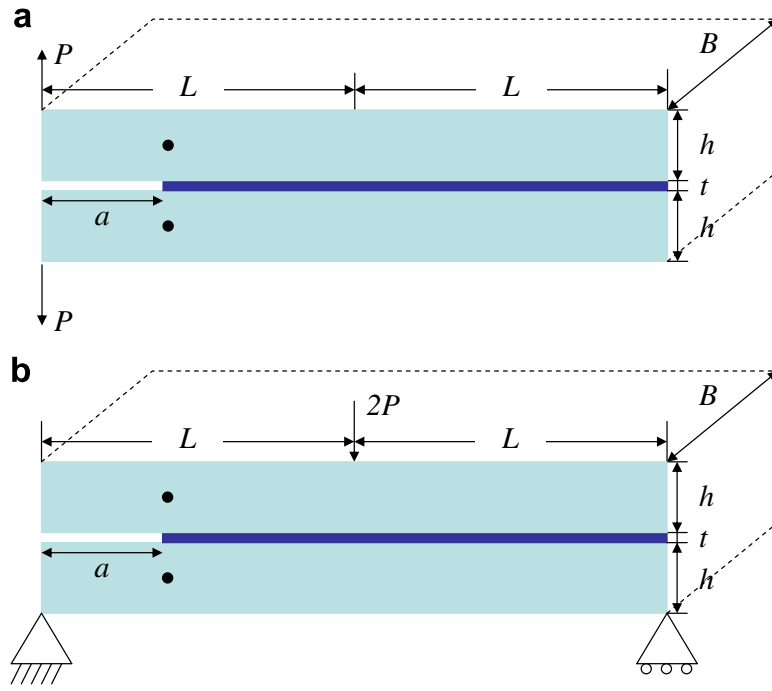


Fig. 2. Schematics of (a) the DCB test configuration and specimen ($L = 75$ mm, $B = 10$ mm, and a ranges from 25 to 70 mm) and (b) the ENF test configuration and specimen ($L = 75$ mm, $B = 10$ mm, and a ranges from 15 to 30 mm). For both configurations $h = 4.76$ mm and $t = 0.7$ mm.

$$J = \int_0^{\tilde{\delta}_n} \sigma(\delta_n) d\delta_n, \quad (2)$$

where δ_n and $\tilde{\delta}_n$ are the normal opening and the normal end-opening of the cohesive zone, respectively, and σ is the normal traction. J reaches a steady-state value, J_{SS} , when $\tilde{\delta}_n$ attains δ_{nc} , the critical normal end-opening. The entire failure process zone is described by the cohesive law. Due to its path independence, the J -integral in Eq. (2) is equal to that obtained by Eq. (1). The normal end-opening $\tilde{\delta}_n$ can be recorded in digital images, thus differentiation of Eq. (2) with respect to $\tilde{\delta}_n$ gives

$$\sigma(\tilde{\delta}_n) = \frac{\partial J}{\partial \tilde{\delta}_n}. \quad (3)$$

Thus, the mode 1 traction–separation law can be obtained by simultaneously measuring the J -integral and the normal end-opening $\tilde{\delta}_n$.

For mode 2 fracture, two configurations were considered: end-notched flexure (ENF) and modified Arcan. The ENF experiments were performed in a three-point bending configuration. The specimen geometry and the load introduction for ENF are shown in Fig. 2(b). The J -integral is given by Leffler et al. (2007)

$$J \approx \frac{9}{16} \frac{(Pa)^2}{Eh^3} + \frac{3}{8} \frac{Pv_0}{h}, \quad (4)$$

where P is the applied load per unit width, a is the crack length, h is the adherend thickness, and E is the elastic modulus of the steel adherends, and v_0 is the shear displacement between the top and bottom adherend/polyurea interfaces at the crack tip. Similar to mode 1 fracture, evaluating J -integral along a path just outside of the failure process zone yields

$$J = \int_0^{\tilde{\delta}_t} \tau(\delta_t) d\delta_t, \quad (5)$$

where δ_t and $\tilde{\delta}_t$ are the tangential opening and the tangential end-opening of the cohesive zone, respectively, and τ is the tangential traction. Differentiation of Eq. (5) with respect to $\tilde{\delta}_t$ gives

$$\tau(\tilde{\delta}_t) = \frac{\partial J}{\partial \tilde{\delta}_t}. \quad (6)$$

However, the ENF configuration can sometimes cause compression of and friction on the crack faces (Carlsson et al., 1986). This problem was quite severe for our case, as will be shown in detail later. Although some methods to reduce the frictional effects have been proposed, such as incorporation of a small steel wire as a spacer between the adherends (Li et al., 2006), the improvement remains unclear. As a result, a modified Arcan shear mode testing technique (Banks-Sills and Sherman, 1991) was considered here as an alternative.

The loading apparatus and the specimen geometry for the modified Arcan are shown in Fig. 3. A circular grip plate with a square window in the center was cut into half along the diameter. A sandwich specimen was screwed into couplings which

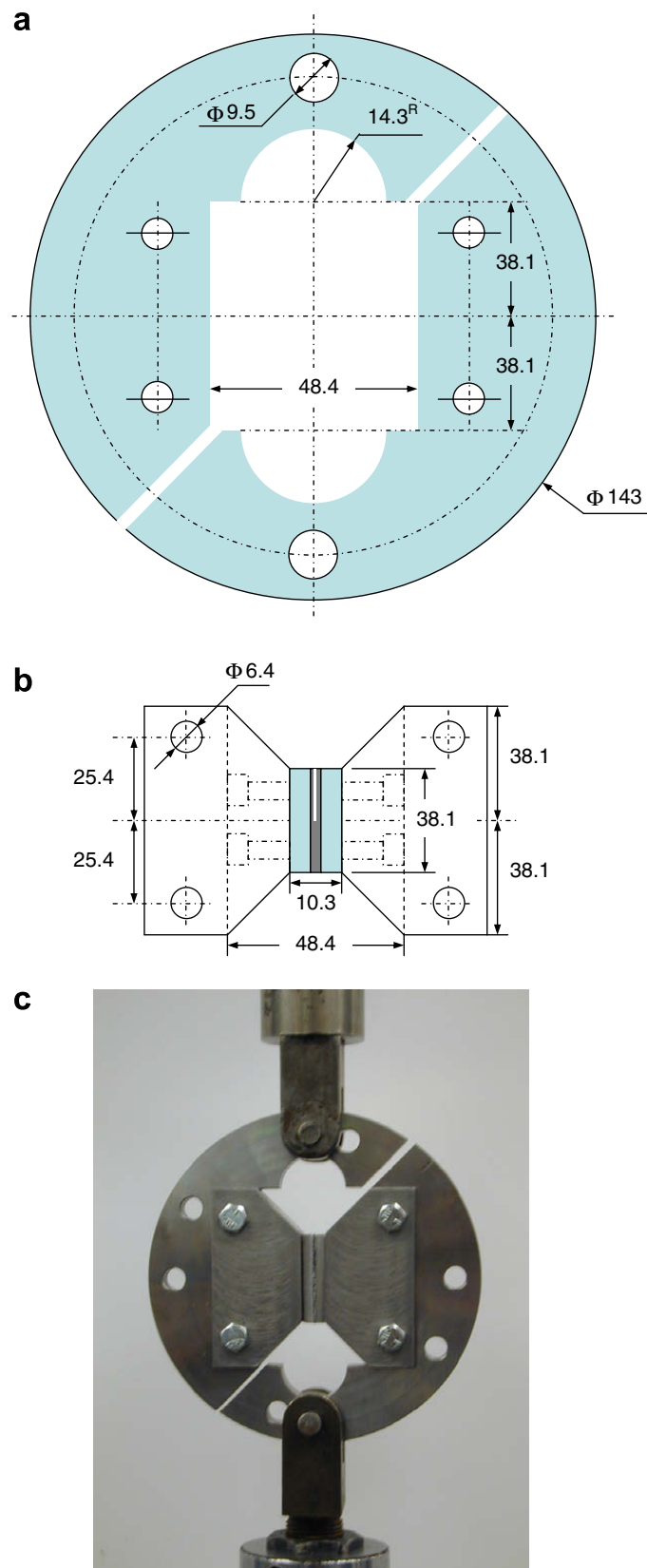


Fig. 3. The grips and specimen for the modified Arcan test for shear fracture, including (a) the circular grips, (b) the couplings with specimen attached, and (c) an optical image of the entire setup. All dimensions are in millimeters.

were attached to the two semi-circular grip plates. Schematics of the circular grip plate and the loading coupling with the specimen, and an optical image of the entire setup are shown in Fig. 3(a), (b), and (c), respectively. The J -integral for the modified Arcan specimen is given (Banks-Sills and Sherman, 1991) by

$$J \approx \eta \frac{A}{Bb}, \quad (7)$$

where η is a constant, A is the area under the load–displacement curve, B is the specimen out-of-plane width, and b is the length of the uncracked ligament. Note that here A is the area under the load–local displacement curve, where the local displacement is the shear displacement across the adhesive layer. Using finite element analysis, it was determined that $\eta = 0.9$ for homogenous aluminum specimens. This value was also used in our study, again considering the path independence of the J -integral for the sandwich configuration. Similarly, the shear traction–separation law was then obtained by recording the J -integral and the shear displacement simultaneously.

The confined tensile and shear experiments also made use of the modified Arcan apparatus just described. The specimens were identical to those used in the mode 2 fracture experiments except that they did not have any cracks. For confined tension, the polyurea/steel interface was perpendicular to the loading direction whereas, for confined shear, the angle was zero.

2.3. Test procedures

All the experiments were conducted at room temperature using a servo hydraulic materials testing system under constant crosshead speed. In all the fracture experiments the end-opening of the cohesive zone was monitored by a CCD camera in real time, which was synchronized with the acquisition of load and displacement data, as shown in Fig. 4. The image resolution is $2 \mu\text{m}$ (corresponding to half pixel in each image). This real-time monitoring scheme can record the entire time and spatial history of the evolution of fracture, e.g., crack blunting, initiation of separation, and crack propagation. Correlation between the recorded fracture events and the load–displacement data provides a means for quantitative understanding of the fracture process. Another advantage of CCD imaging is that it records the exact end-opening of the cohesive zone. The opening comprises both bulk deformation of the adhesive layer and the separation across the cohesive zone. In other methods where, for example, extensometers are used (Sorensen, 2002), the measured end-opening includes part of the adherend deformation although this deformation is often assumed to be small.

In addition, CCD imaging was required for accurate measurements of displacement and strain in both the original and modified Arcan experiments. The displacement imposed on the specimen is not equal to the crosshead displacement, due to machine and grip compliance. With the CCD imaging, the local displacement and thus strain can be directly obtained. Both the displacements measured from CCD imaging and the crosshead movement are plotted in Fig. 5 for two cases: confined tension and confined shear on the sandwich specimens, respectively. As can be seen, the strain determined from the crosshead displacement is inaccurate especially at the beginning of the experiment when the displacements are small. The differences were particularly noticeable under tensile loading and reliance on crosshead displacements would clearly lead to low measurements of moduli. It should be noted that all the image analyses were conducted after the experiment.

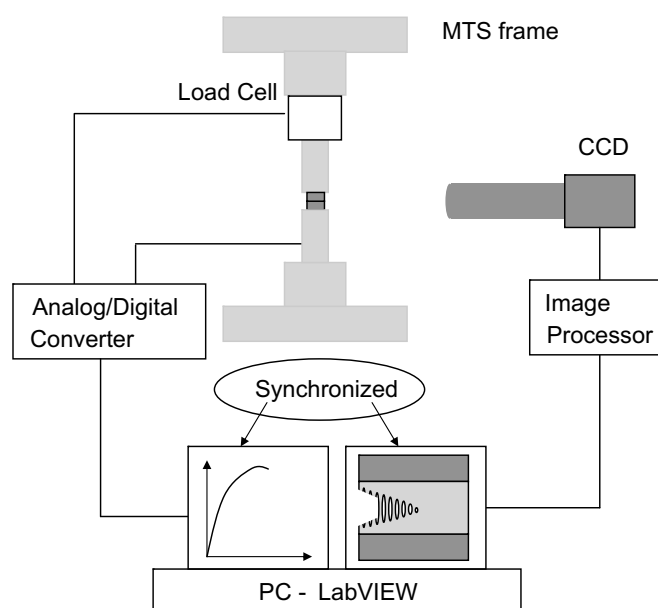


Fig. 4. A schematic of the apparatus shows both data and image acquisition systems.

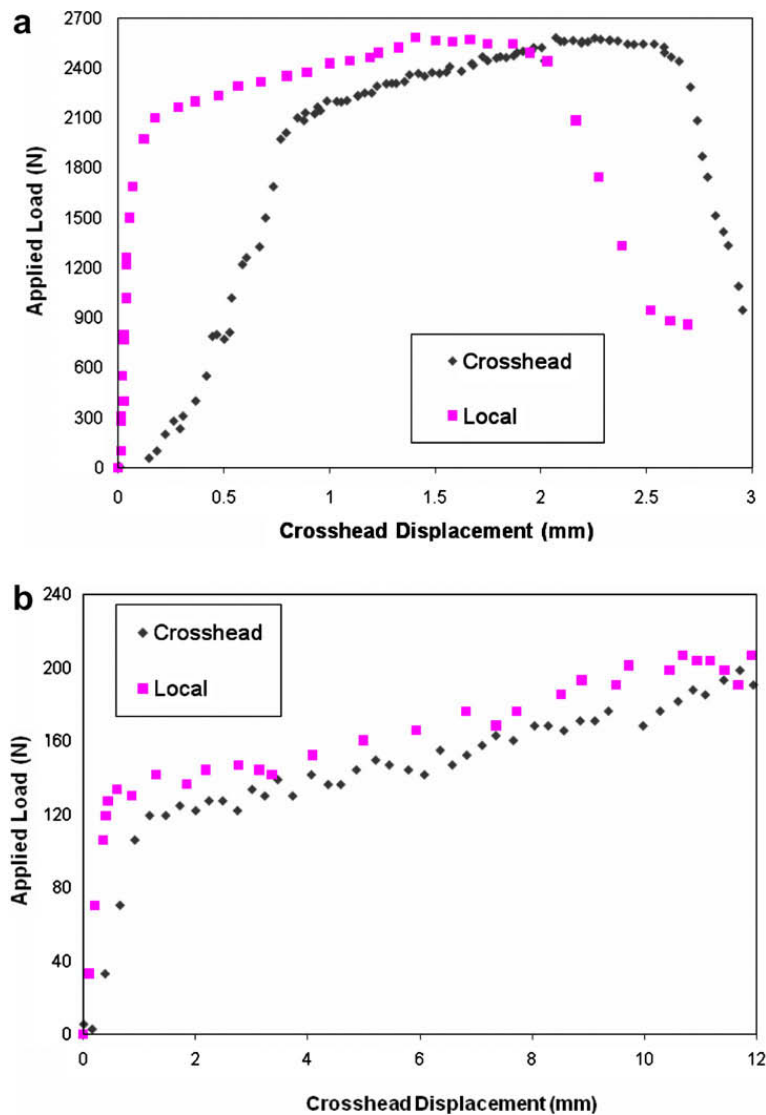


Fig. 5. Displacement measured from CCD images and crosshead displacement for (a) confined tension and (b) confined shear of polyurea/steel sandwiches.

3. Results

3.1. Uniaxial tension and shear behavior of polyurea

Polyurea specimens were characterized in uniaxial tension at three strain rates (0.001 , 0.01 , and 0.1 s^{-1}). The specimens exhibited (Fig. 6) rate-dependent, nonlinear stress–strain behavior. The initial moduli were slightly dependent on the strain rate; by contrast, the stress level at which softening occurred was quite rate-dependent, increasing with increase in strain rate. The initial modulus of the polyurea was $192 \pm 10 \text{ MPa}$.

The nonlinear shear stress–shear strain behavior of polyurea at 0.001 , 0.01 , and 0.1 s^{-1} is shown in Fig. 7. All the specimens were loaded to failure. Similar to the uniaxial response, the initial shear moduli were slightly dependent on the strain rate; in contrast, the stress level at which softening occurred was quite rate-dependent. The initial shear modulus of the polyurea was $36.5 \pm 5 \text{ MPa}$. Note here the shear strain was determined from the CCD imaging. In fact using the crosshead displacement led to an overestimate in the shear strain of 100% and thus a corresponding underestimate in the shear modulus.

3.2. Tension and shear behavior of sandwich specimens

The tension and shear experiments on the sandwich specimens were conducted at nominal strain rates of 0.03 and 3 s^{-1} . In contrast to the monolithic specimens, the initial moduli depended on the loading rates for both tension and shear (Figs. 6 and 7). In tension, the added constraint in the sandwich specimens excites more of a bulk response, which should lessen, rather than increase, the time dependence of the response of a viscoelastic material. However, the bulk polyurea was not

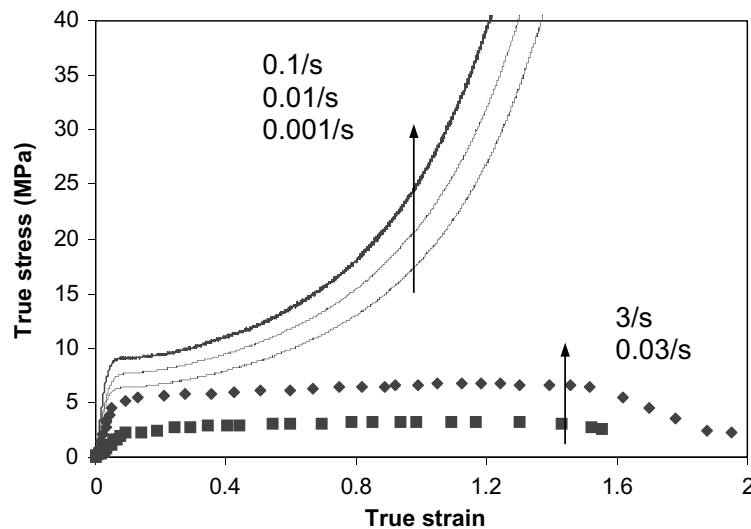


Fig. 6. Stress–strain curves of polyurea under uniaxial tension at different strain rates. The dashed lines are for confined tension of sandwich specimens (0.03 and 3 s^{-1}) and the solid lines are for uniaxial tension (0.001 , 0.01 , and 0.1 s^{-1}).

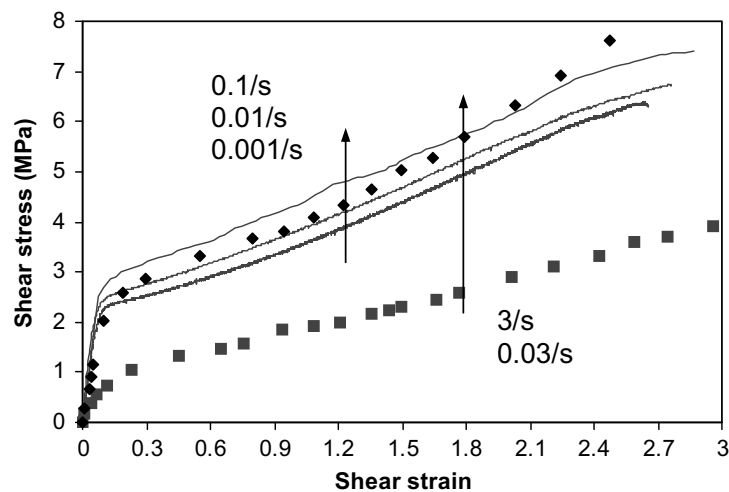


Fig. 7. Stress–strain curves of polyurea under shear at different strain rates. Dashed lines are for shear of sandwich specimens (0.03 and 3 s^{-1}) and solid lines are for shear of butterfly specimens (0.001 , 0.01 , and 0.1 s^{-1}).

the only possible source of time dependence in the sandwich specimens: the polyurea/steel interface could also have been a contributor, both in tension and shear, through an interphase region.

In the sandwich specimens under tension, the softening stress level occurred at 2 and 5.5 MPa, which was lower than the values for the uniaxial tensile specimens, which ran from 6 to 9 MPa over the strain rates that were imposed. The strain rates in the sandwich specimens ranged from 0.03 to 3 s^{-1} , which means that neither the higher strain rates nor the higher constraint in the sandwich specimens raised the softening stress level. This again suggests that the stress–strain response of the sandwich specimens in Fig. 6 is that of the interface and the lower knee stress levels are an indication of the onset of some form of damage at the interface. This also explains the lower rate of increase in stress levels after the softening stress level compared to the monolithic specimens. At both displacement rates, macroscopic debonding occurred at the maximum stress levels, presumably due to the coalescence of damage.

Under shear, the softening stress levels for the sandwich specimens were lower than had been observed in the monolithic specimens, particularly at the lower rate. This might again be taken as being due to the occurrence of debonding in the sandwich specimens. However, the rate of increase in stress after softening was the same in monolithic and sandwich specimens, which suggests that debonding did not occur prior to the maximum stress.

3.3. Mode 1 fracture

The results of a typical experiment with the DCB specimens are shown in Fig. 8. The variation of the J -integral with the normal end-opening displacement at a loading rate of 0.2 mm/s is shown first (Fig. 8(a)). The J -integral increased with

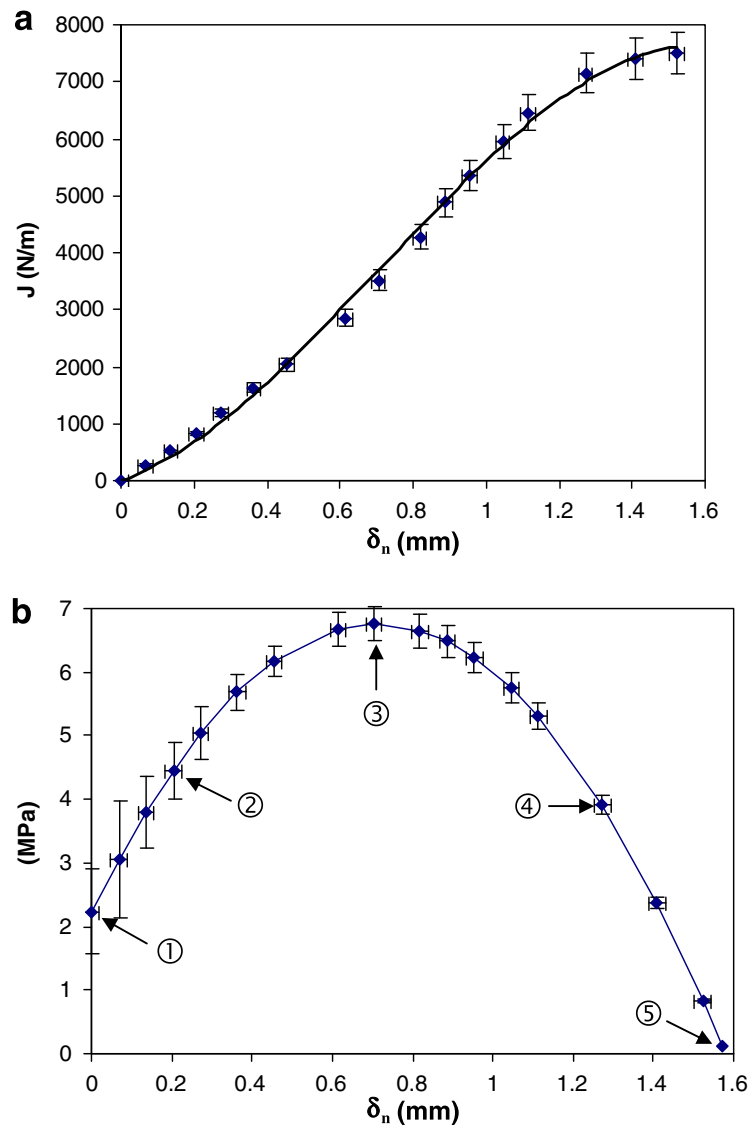


Fig. 8. (a) A typical J - δ_n response and (b) traction-separation law in opening mode fracture. δ_n in both figures is the normal displacement. The strain rate is 0.3 s^{-1} .

increasing normal displacement, reaching a steady-state value, J_{SS} . Three methods were employed for numerical differentiation of J with respect to δ_n , including moving average, piecewise fitting and global fitting. They yielded very similar results. Details of these methods are given in Appendix. For convenience of writing the traction-separation laws explicitly, the global fitting method will be used in the rest of the paper. A cubic polynomial fit the J - δ_n response very well and then differentiation with respect to δ_n provided the traction-separation law, as shown in Fig. 8(b). The error bars reflect estimates of the errors involved in determining J , σ and δ_n . The traction-separation laws shown later in the paper were all obtained as averages from 3–4 runs per specimen at different crack lengths.

The entire failure process of the specimen was recorded in accordance with the J -integral measurement. Fig. 9 shows several representative photographs at progressive stages of deformation. Each subfigure corresponds to the stage numbers (?) identified in the traction-separation law (Fig. 8(b)). The initial crack prior to loading ① is shown in Fig. 9(a). The onset of blunting ② can be seen in Fig. 9(b) as the cohesive stress was increasing and small voids could be seen developing in the cohesive zone. Further blunting can be seen (Fig. 9(c)) accompanied by void growth and the initiation of debonding at the upper interface slightly ahead of the pre-crack, corresponding to stage ③. Since this is a nominally mode I experiment, interfacial debonding occurs when the stress normal to the interface σ_{22} exceeds the bond strength. The bond strength is equal to the peak cohesive stress σ_0 . In Fig. 9(d), the crack blunting was severe. Although the crack opening was more pronounced, it did not propagate. The existing voids grew further and more voids started to appear during stage ④ where the cohesive stress was decreasing. The final stage ⑤ of the separation process corresponds to zero cohesive stress and the growth of the interfacial crack, as shown in Fig. 9(e).

Specimens were tested at four loading rates and, for each rate, there was some specimen-to-specimen variation in the J - δ_n curves, particularly at small and large openings. The variation at small openings might have been due to variations in the

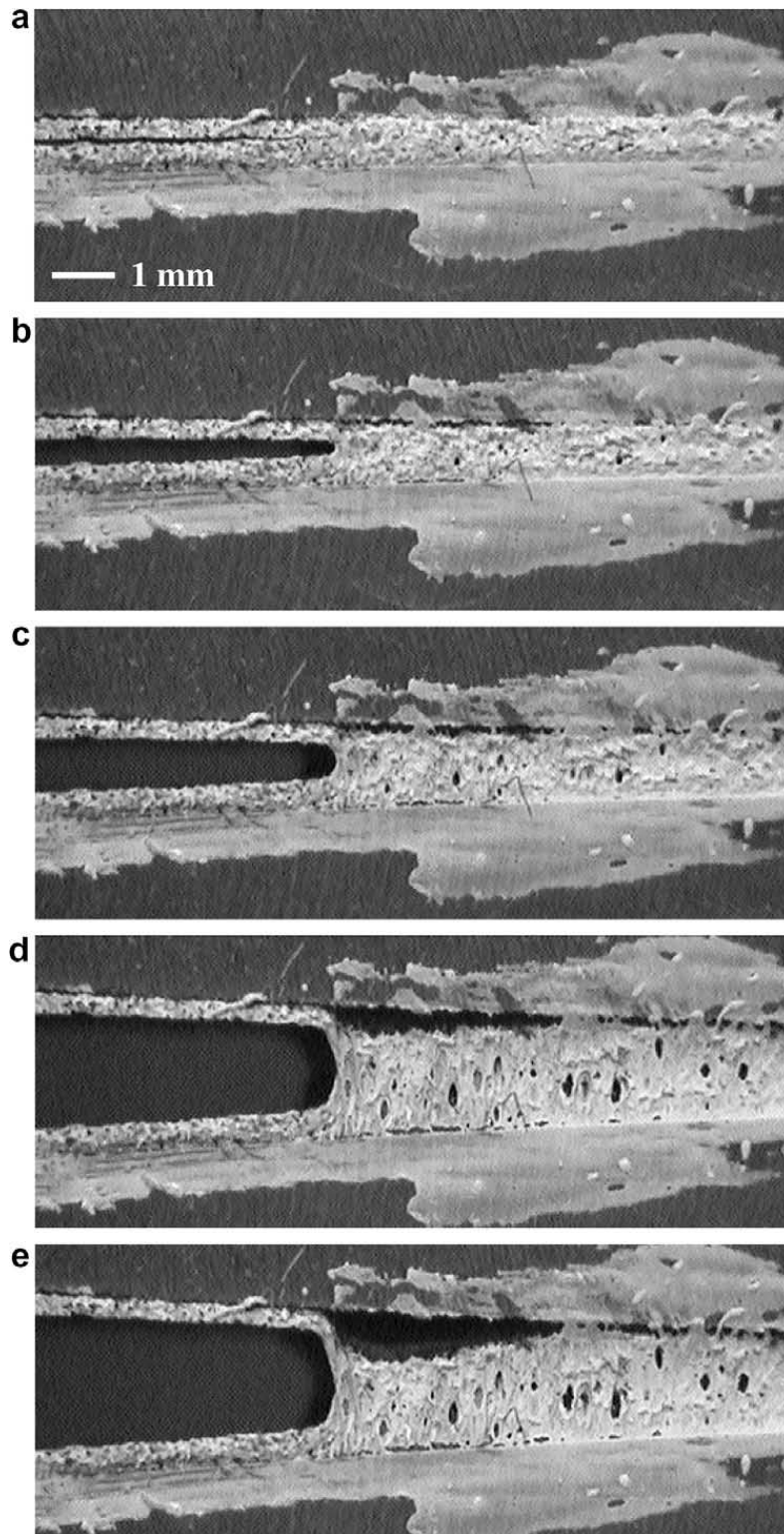


Fig. 9. The entire sequence of the failure process of a polyurea/steel sandwich specimen in opening mode fracture. The images correspond to the different stages in the traction–separation law as shown in Fig. 8b.

initial crack sharpness, or experimental error in displacement measurements. The variation at large opening displacements might have been caused by variations in the failure process zone evolution as described later. Fig. 10(a) plots the average of the fitted cubic polynomials for J – δ_n curves at each loading rate while the corresponding traction–separation laws appear in Fig. 10(b). The effect of loading rate on the traction–separation law was pronounced. The peak cohesive stress was about 1.8 MPa for the slowest loading rate (0.002 mm/s) and about three times higher for the highest loading rate (5 mm/s). In the meantime, δ_{nc} (critical end-opening displacement) decreased from about 2.4 mm to nearly 1 mm. Even though the

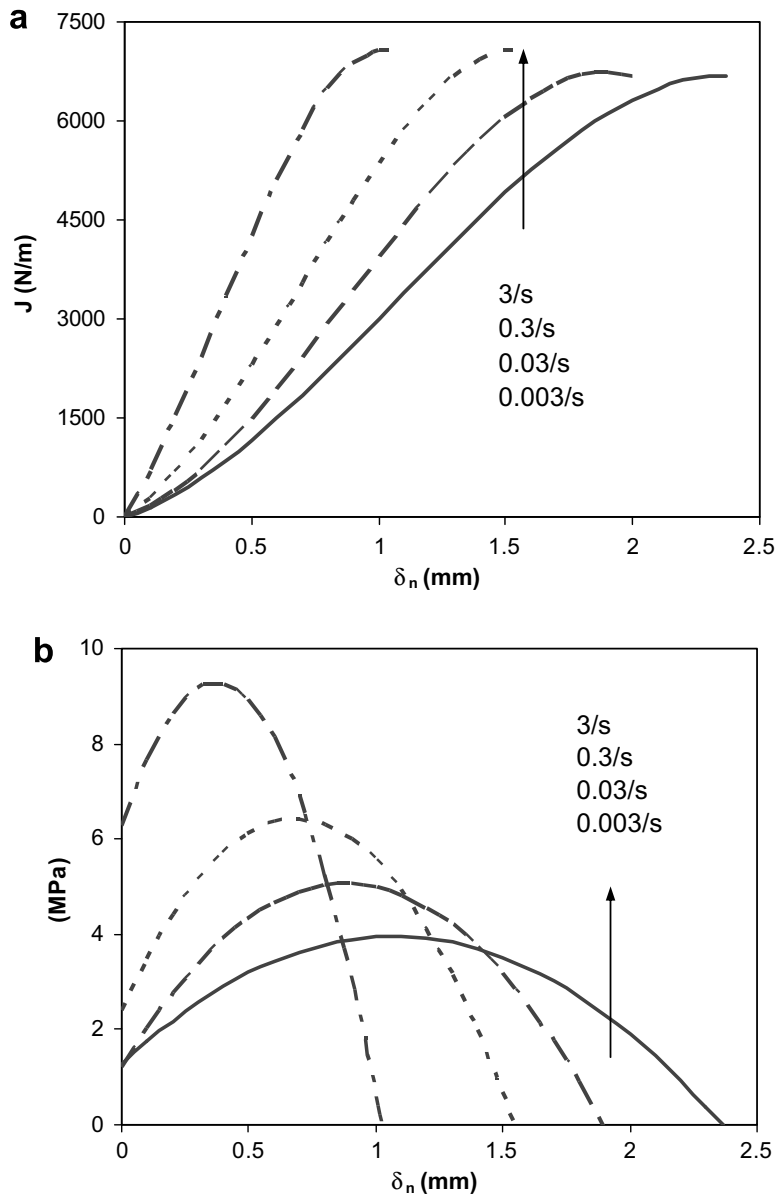


Fig. 10. (a) J - δ_n curves and (b) traction-separation laws for opening mode fracture at different loading rates. δ_n in both figures is the normal displacement.

shapes of all the cohesive laws followed quadratic polynomials, the details were quite different for each loading rate. For the slowest loading rate the cohesive stress rose to its peak at a fairly large crack opening (~ 1.1 mm); by contrast, for the highest loading rate the cohesive stress rises rapidly to the peak stress.

The cohesive law at each loading rate can be expressed by a quadratic polynomial, similar to the polynomial cohesive law proposed by Needleman (1987). It can be written as

$$\sigma(\delta_n) = -\frac{\sigma_0}{(\delta_{nc} - \delta_{n0})^2}(\delta - \delta_{n0})^2 + \sigma_0, \quad (8)$$

where σ_0 is the peak cohesive stress, δ_{nc} is the critical end-opening displacement, and δ_{n0} is the end-opening displacement at which the cohesive stress reaches σ_0 . The values of the parameters σ_0 , δ_{n0} , and δ_{nc} for all the loading rates at mode I fracture are given in Table 1.

3.4. Mode 2 fracture

The results from the ENF experiments are presented first. Fig. 11(a) is an image of a crack in an ENF specimen. Using digital image correlation (DIC), we found that, behind the crack tip, there was a compressive strain perpendicular to the interface of about 5% (Fig. 11(b)), distributed quite evenly along the crack faces. This resulted in frictional loading of the crack faces (Fig. 11(c)). In addition, the ENF specimen only provides a relatively small shear displacement that was not sufficient

Table 1
Parameters for the quadratic traction–separation law equation (8) as a function of loading rate and mode

Rate (s^{-1})	$\Gamma 1$ (kJ/m^2)	σ_0 (MPa)	δ_{n0} (mm)	δ_{nc} (mm)	$\Gamma 2$ (kJ/m^2)	τ_0 (MPa)	δ_{tc} (mm)
0.003	6.69	3.95 ± 0.06	1.21 ± 0.02	2.36 ± 0.04	–	–	–
0.03	6.68	5.12 ± 0.15	0.92 ± 0.04	1.90 ± 0.08	8.29	2.72 ± 0.12	4.15 ± 0.15
0.3	7.08	6.45 ± 0.35	0.76 ± 0.05	1.56 ± 0.13	11.26	5.45 ± 0.25	3.18 ± 0.20
3.00	7.08	9.25 ± 0.60	0.41 ± 0.02	1.02 ± 0.05	13.44	6.97 ± 0.46	3.02 ± 0.16

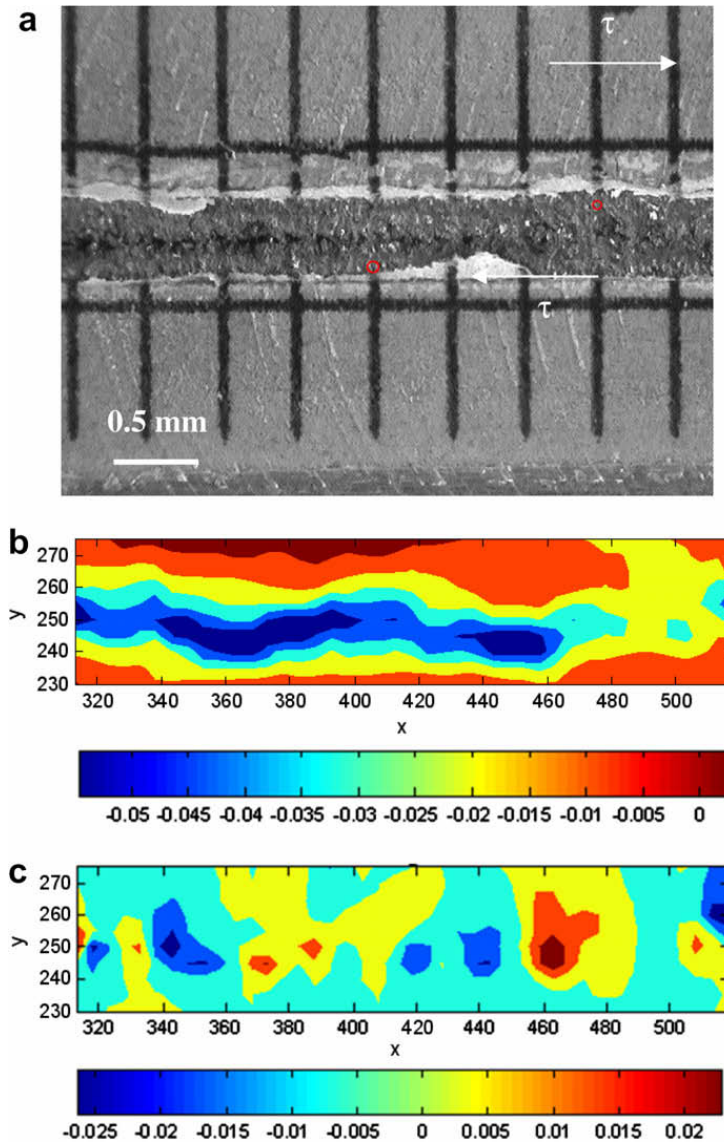


Fig. 11. (a) The crack tip region in an ENF specimen the two red dots define a rectangular area that is analyzed using DIC and plotted in (b) and (c), (b) the through-thickness compressive strain behind the crack front, and (c) the through-thickness frictional loading along the crack faces. The scale bars in (b) and (c) show the strains in vertical and horizontal directions, respectively. (For interpretation of the references to colours in this figure legend, the reader is referred to the web version of this paper).

to heavily deform and damage the highly deformable polyurea. These issues motivated the consideration of the Arcan configuration, which can provide large shear displacements.

A modified version (Popelar and Liechti, 2003) of the original Arcan configuration (Arcan et al., 1978) was considered here. The J – δ_t curves and the shear traction–separation laws at three loading rates, are given in Fig. 12(a) and (b), respectively. Similar to the mode 1 fracture experiments, J increased with increasing δ_t , reaching a steady-state value J_{SS} . Here, the J – δ_t curves could not be fitted well with a polynomial so a piecewise fitting algorithm was employed to obtain the traction–separation law. The entire crack initiation and propagation process was also recorded. Fig. 13 shows representative images of different stages in the deformation of a specimen loaded at a nominal strain rate of $3 s^{-1}$. In Fig. 13, stage ① shows

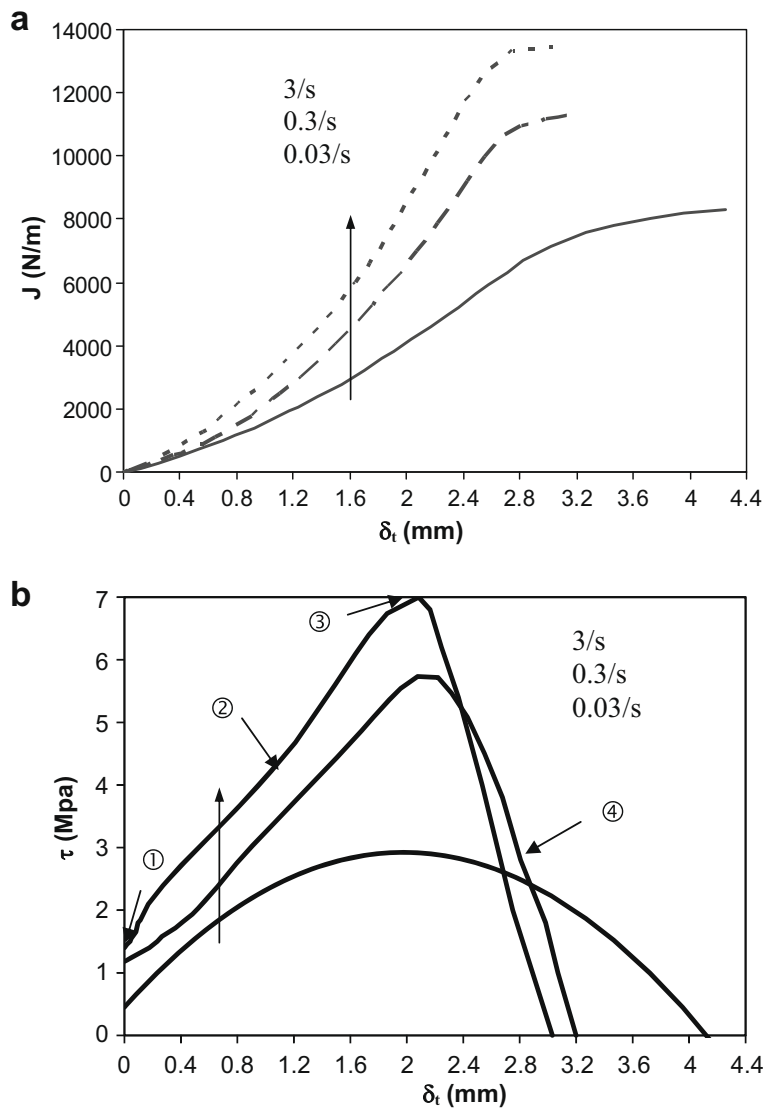


Fig. 12. (a) J - δ_t curves and (b) traction-separation laws for shear fracture at different loading rates. δ_t in both figures is the shear displacement.

the initial crack prior to loading (corresponding to ① in Fig. 12(b)). An intermediate stage ② illustrates the onset of localized stretching from the crack tip to the right interface as the cohesive stress increased. This can be seen as the region with oriented texture emanating from slightly behind and extending ahead of the crack tip. Further stretching ahead of the crack tip appears in stage ③ together with debonding along the interface in front of the crack tip corresponding to the peak cohesive stress. At stage ④, the polyurea around the crack tip was partially retracted due to the onset of the debonding, and the cohesive stress decreased. The interfacial debonding resulted in unloading of the adjacent adhesive layer, and the debonding itself propagated in a catastrophic manner. The peak shear stress τ_0 and the critical shear displacement δ_{tc} for all the loading rates are given in Table 1.

The images in Fig. 13 suggest that the crack did not advance under shear stress; instead the interfacial debonding occurred due to the normal component of the stretching exceeding the bond strength. The local strain field ahead of the crack tip was therefore evaluated using DIC. The shear displacement fields and corresponding strains are presented at several load levels. Fig. 14(a) and (b) provide contours of the displacement component parallel to the interfaces and engineering shear strain, respectively. Concentration of the strain near the crack tip can be clearly identified. The shear strain profiles at three load levels (Fig. 14(c)) along a line starting from the crack tip shows the concentrations near the crack tip and the decay to the nominal values (dashed line) beyond approximately two layer thicknesses. At all load levels, the maximum shear strain appeared to be nearly 1.5 times the uniform strain.

4. Discussion

In this section, we discuss the form and rate dependence of the traction-separation laws and how they may be related to the time dependence of bulk polyurea and porosity.

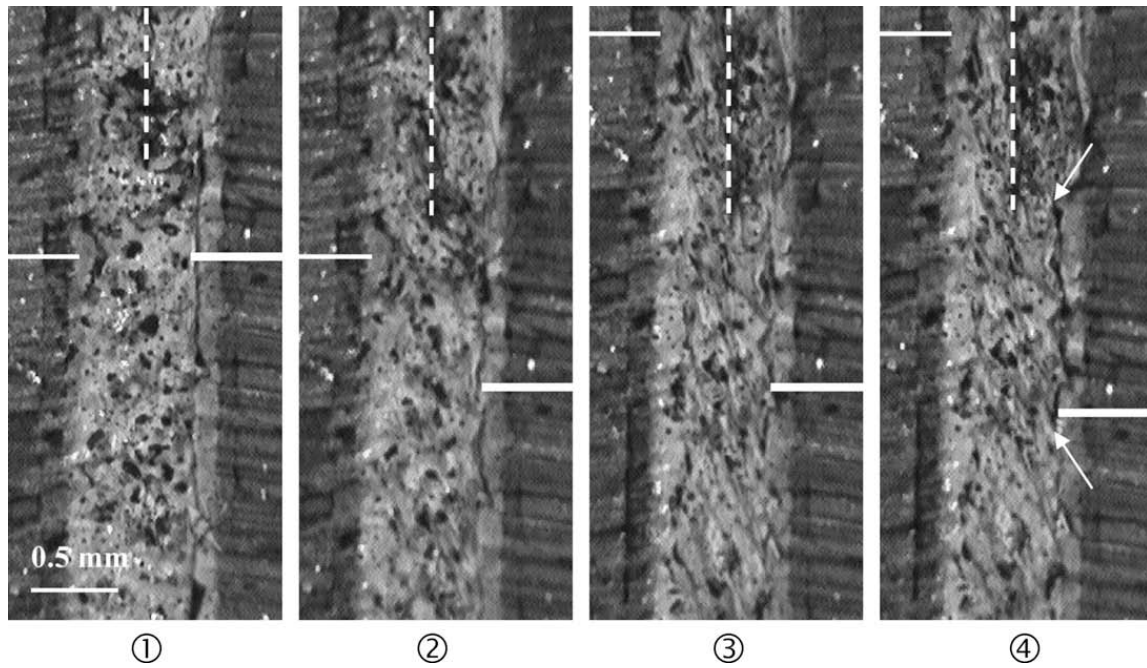


Fig. 13. The entire sequence of crack initiation in a sandwich specimen under shear loading. The images are in accordance with the different stages identified in Fig. 12(b). A dashed vertical line in each subfigure is drawn to highlight evolution of the initial crack. Two solid horizontal lines moving with the two adherends show the relative displacement between the adherends in order to illustrate the shear deformation in the polyurea. In ④, two arrows on the right side of the polyurea/steel interface mark the tips of an interfacial crack.

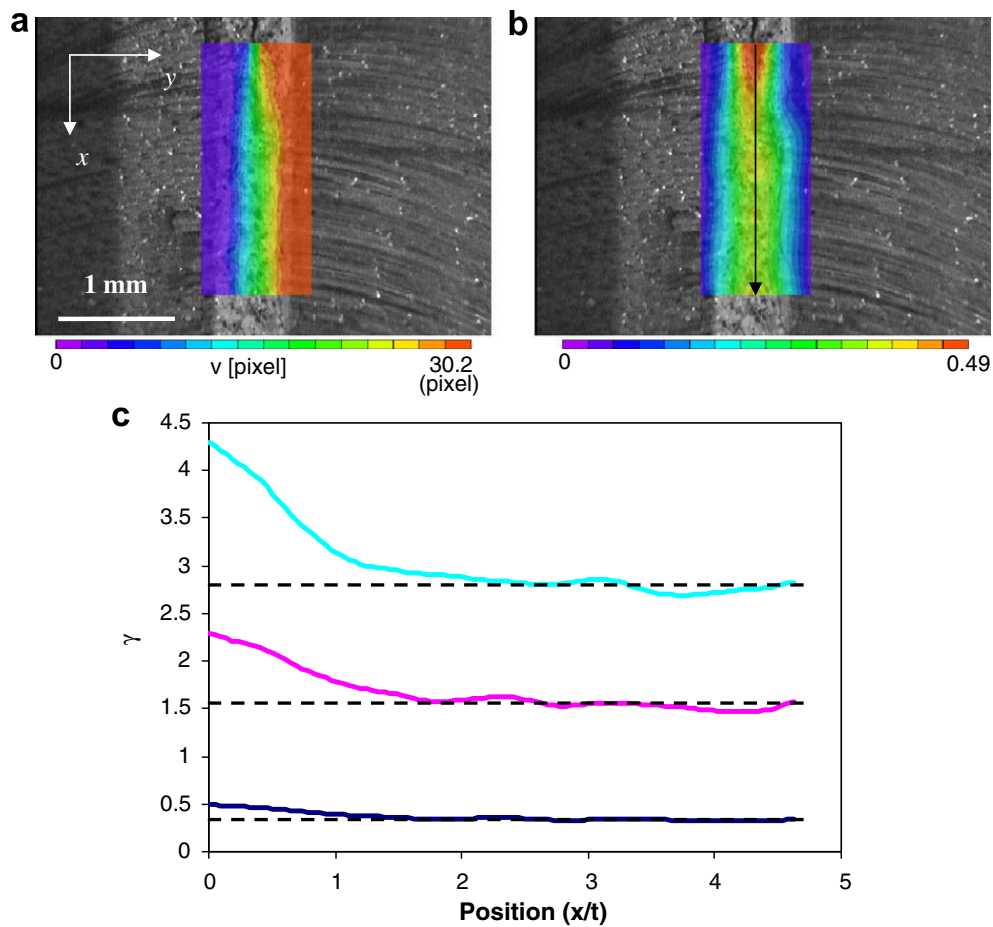


Fig. 14. (a) Shear displacement contours, (b) engineering shear strain contours, and (c) engineering shear strain as a function of distance from the crack tip. Dashed lines are the nominal shear strains. The three strain profiles correspond to images ①, ② and ③ in Fig. 3.

Table 2
Comparison of softening stress with maximum traction levels

Softening stress			Maximum traction			Ratio	
Rate (s^{-1})	Tension σ_s (MPa)	Shear τ_s (MPa)	Rate (s^{-1})	Normal σ_0 (MPa)	Shear τ_0 (MPa)	Normal σ_0/σ_s	Shear τ_0/τ_s
0.001	6.39	2.37	0.003	3.95	2.92	0.62	1.23
0.01	7.69	2.53	0.03	5.12	5.72	0.67	2.26
0.1	9.01	2.86	0.3	6.45	7.01	0.72	2.45
			3.00	9.25			

4.1. Shape

The most striking feature of the traction–separation laws shown in Figs. 10 and 12 is the nonzero stress at zero crack opening. This has been observed before by Sorensen (2002) who used the same method to determine the traction–separation laws associated with adhesive joints consisting of polyurethane and steel. It has also been assumed in traction–separation laws that have been extracted iteratively (Swadener and Liechti, 1998; Shirani and Liechti, 1998; Mello and Liechti, 2006). Jin and Sun (2005) recently provided a theoretical basis for this feature, arguing that it is needed in order to remove the singularity at the crack tip. At the same time, it seems unlikely that a real material would have a step increase in traction near zero displacement, which then relates to questions about the resolution of the technique. The resolution of the displacement technique was 2 μm , two orders of magnitude less than the scale interval in Fig. 8 and one order of magnitude better than is needed for resolving modulus. However, the differentiation process to obtain the tractions can cause significant scatter in data, as is shown in Fig. A1 of Appendix. Consequently, a polynomial fitting to the J -integral was employed, which provided a smooth traction–separation law but might be smearing some details, especially in the initial stages of loading. Nonetheless, all three techniques did point to a sharp increase in stress near zero displacement.

Jin and Sun further suggested that the maximum traction ranges from 1.15 to 2.5 times the yield strength of the material for perfectly plastic to mildly strain hardening materials (hardening exponent of 0.2). For comparison, the ratios of the maximum tractions to the softening stress levels that were obtained in the present study are shown in Table 2. For mode 1 fracture and uniaxial tension, the ratios were less than one. This simply suggests that, in tension, the interface is weaker than the bulk material. Under shear, the ratios ranged from 1.23 to 2.45, which is in the range suggested by Jin and Sun. Interestingly, the shear stress–strain behavior of the bulk polyurea was more like a metal than the tensile stress–strain behavior, which exhibited the usual softening followed by stiffening behavior of polymers. The overall shapes of the traction–separation laws changed with loading rate and fracture mode. Tvergaard and Hutchinson (1993) suggested that effect of the shape on the fracture process was relatively unimportant. However, Gu (1995) found that the shape of bridging laws did affect crack growth calculations in fiber-reinforced ceramics and Jacobsen and Sørensen (2001) made similar observations in mode I intralaminar crack growth in fiber-reinforced polymers. A recent reexamination of this issue (Jin and Sun, 2005) suggests that the shape governs the cohesive zone size and what was termed “the apparent energy release rate of LEFM”, a quantity that approaches the cohesive energy density when crack extensions are significantly greater than the cohesive zone size.

4.2. Rate dependence

In Section 3.1, it was noted that, under uniaxial tension and shear, the polyurea exhibited slight rate dependence prior to softening and considerably more thereafter. The response of the sandwich specimens was much more time dependent prior to and following softening, which suggested that the interface was playing a role. The initial portion of the mode 1 and 2 traction–separation laws also exhibited significant levels of rate dependence. In view of the interfacial nature of the crack growth in the specimens, this suggests that the traction separation laws are reflecting the time dependence of the interphase region. In fact, if the tensile and shear response of the sandwich specimens is plotted alongside the corresponding traction–separation law (Fig. 15), there is a remarkable resemblance between them further strengthening the argument that the traction–separation laws determined here represent the behavior of the interphase. In addition, the strain rates are amplified at the interfacial crack fronts, which would bring the response of the polyurea further into the viscoelastic regime.

The area under the traction–separation law or the intrinsic toughness Γ is considered as a function of the nominal strain rate in Fig. 16. The mode 1 toughness values were consistently lower than the mode 2 values and displayed very little dependence. The mode 2 toughness was much more rate dependent; nearly double the mode 1 value at the highest rate. Although mode 2 experiments were not conducted at the lowest rate ($0.003 s^{-1}$), the trend of the data suggests that the mode 1 and 2 toughness values could be quite similar there. The greater influence of strain rate in shear is not surprising given the dilatational contribution to mode 1 and the shorter viscoelastic spectrum in the bulk relaxation modulus of the polyurea.

4.3. Failure mechanisms

As observed in Fig. 9, the initial cohesive crack did not propagate under mode 1 loading; rather an interfacial debond occurred ahead of it despite the fact that the stress at the crack tip is higher than that at the debonding site. This indicates that the interface was relatively weak compared to the cohesive strength of the polyurea. Similar observations were made for

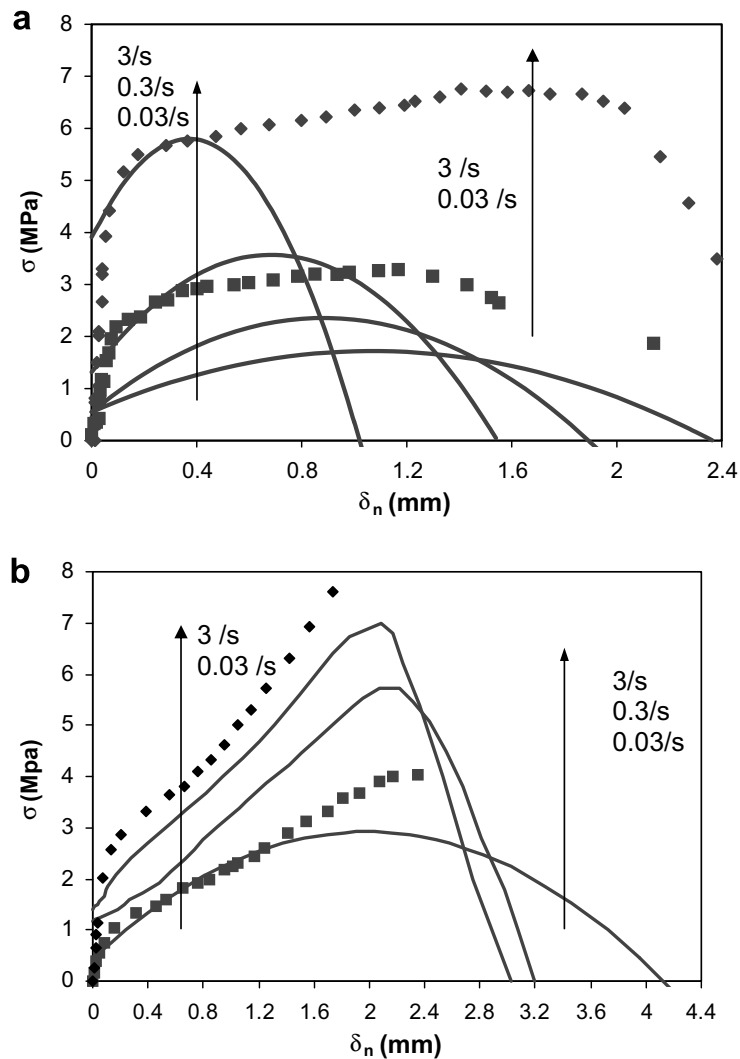


Fig. 15. The response of uncracked sandwich specimens is compared with traction–separation laws obtained under (a) tension and (b) shear. For both tension and shear, the dashed lines are for uncracked sandwich specimens at 0.03 and 3 s⁻¹ and the solid lines are for the fracture experiments at 0.03, 0.3, and 3 s⁻¹.

mode 2 fracture (Fig. 13). The initial crack did not propagate perpendicular to the direction of the maximum tangential stress. Instead, the material between the crack tip and both interfaces stretched as can be seen from the texture that developed at roughly 45° to the original direction of the crack. Interfacial debonding occurred at the intersection of the texture and either interface, either ahead of or slightly behind the original crack tip.

This failure mechanism for mode 2 fracture is quite different from observations in the literature (Chai and Chiang, 1996; Shih et al., 1991). For a brittle adhesive, micro cracks opened up ahead of the initial crack and grew in the direction normal to the maximum principal stress direction. For a ductile adhesive, a number of failure modes have been reported. If the initial crack is at an interface: (1) the crack can propagate along the same interface; (2) a micro debond can occur on the other interface ahead of the crack tip; (3) it can kink to the other interface and later form a micro debond on the initial interface or (4) a void can nucleate in the adhesive layer ahead of the crack tip. If the initial crack is in the middle of the adhesive layer: (1) it can kink to one interface and exhibit the behaviors just mentioned or (2) a void is nucleated in front the crack tip. In view of the fact that the polyurea can be stretched for several hundred percent, the failure mechanism for polyurea/steel interface belongs to the category of ductile failure.

For ductile adhesive joints under mode 1 loading, there are four fracture mechanisms: (1) near-tip void growth and coalescence; (2) interfacial debonding near the crack tip; (3) cavitation induced by high triaxiality ahead of the crack tip; and (4) interfacial debonding ahead of the crack tip. Schematics of these four mechanisms are sketched in Fig. 17. Fracture mechanism 1 is commonly observed in the ductile fracture of homogeneous materials. When the crack tip blunts to an opening of the order of the mean spacing between voids, the voids are wholly within the finite strain zone so that void-crack coalescence is imminent. Fracture mechanism 2 occurs when the near-tip stress normal to the interface σ_{22} exceeds the bond strength of the weak interface. Fracture mechanism 3 is due to cavitation at a distance of several adhesive layer thicknesses ahead of the crack tip. The remote triaxiality develops when the interfacial bond is sufficiently strong to allow the ductile

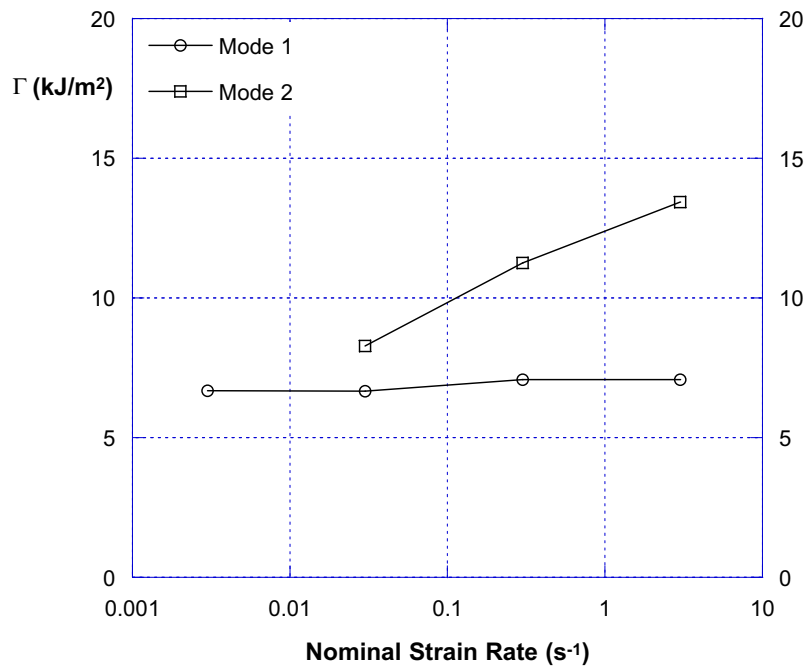


Fig. 16. The intrinsic toughness in mode 1 and mode 2 as a function of the nominal strain rate.

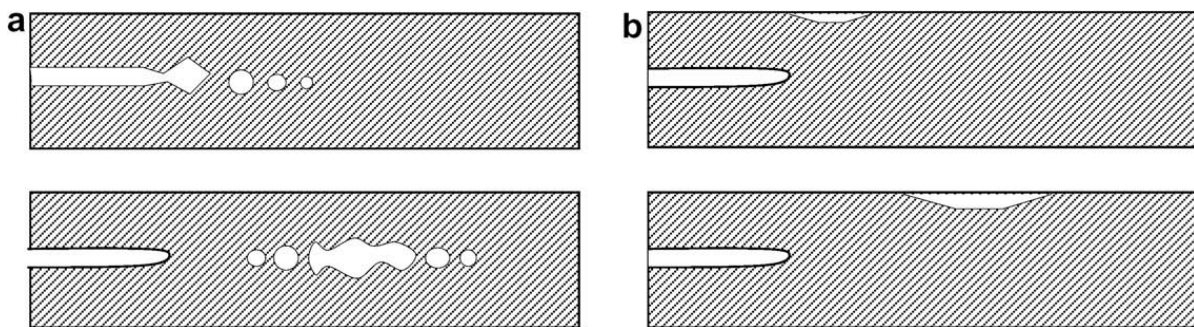


Fig. 17. Four typical fracture mechanisms in a ductile adhesive joint. (a) Near-tip void growth and coalescence; (b) interface debonding near the crack tip; (c) high triaxiality cavitation ahead of the crack tip and subsequent coalescence; and (d) interface debonding ahead of the crack tip.

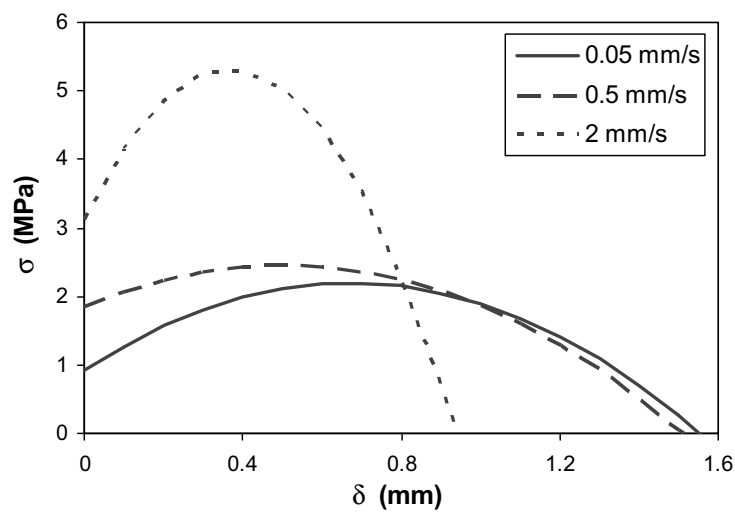


Fig. 18. Traction–separation laws for opening mode fracture of the second batch (porous polyurea) at different loading rates. δ_t is the shear displacement.

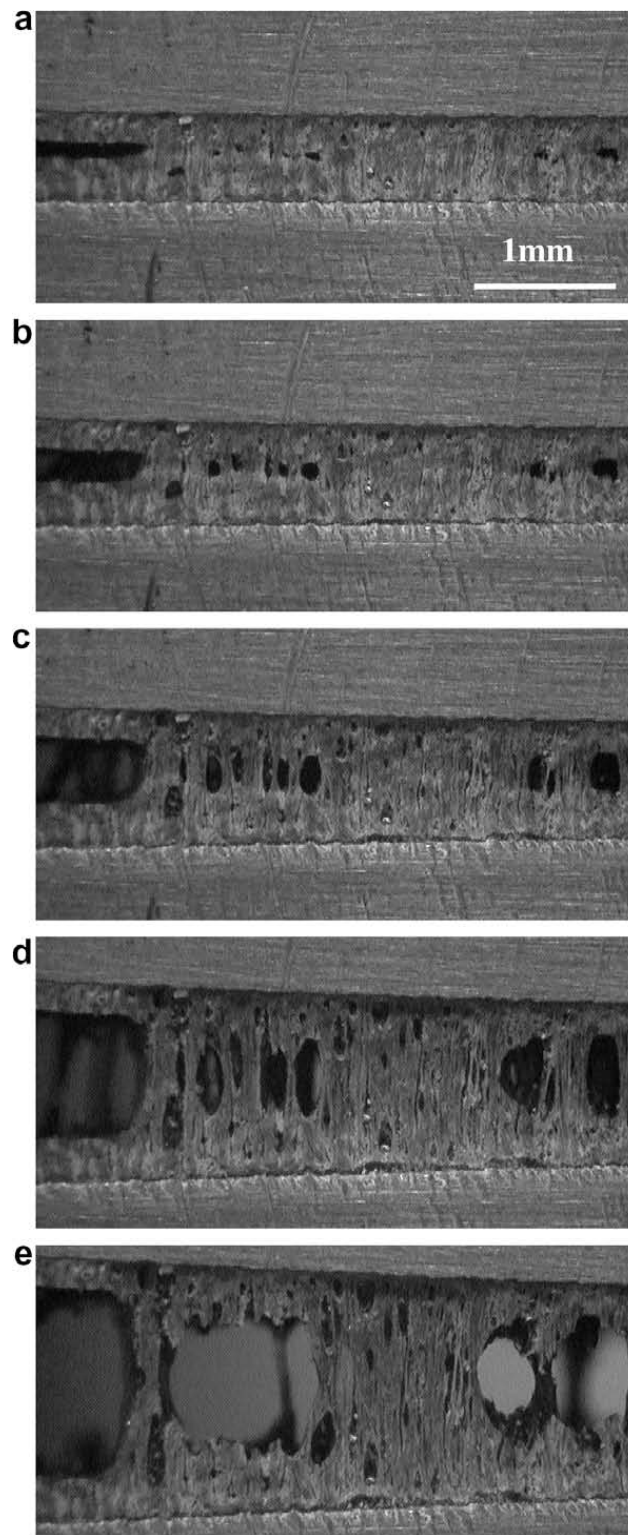


Fig. 19. Entire sequence of the failure process of a porous adhesive joint in opening mode fracture. The images are in accordance with the different stages in the traction separation law as shown in Fig. 17 (loading rate 0.2 mm/s).

layer to undergo substantial plastic deformation. Detailed analyses and comparison with experiments for each fracture mechanism are beyond the scope of this paper. Interested readers can refer to the analyses for similar sandwiched systems provided in Shih et al. (1991) for mechanism 2 and in Choi et al. (2001) and Varias et al. (1991) for the other three mechanisms. Mechanism 2 is the one that was observed in our experiments here. Our experimental results for mode 1 fracture can be categorized as the second fracture mechanism. However, if significant levels of porosity are introduced in the adhesive layer, the failure mechanism may be different, as is now discussed in the following section.

4.4. Effects of the polymer porosity

The spray process that was used in forming the polyurea layer introduced a large number of voids (pores) in the material. The volume fraction of the porosity and the distribution of pore sizes depend on the exact chemical formulation and conditions of the spray process (such as temperature and humidity). In addition, because of the manner in which the sandwich was constructed, there are more pores along the mating surfaces. In order to examine the effect of porosity, we conducted the same fracture tests on another batch of sandwich specimens that consisted of more porous polyurea. We used density as the parameter to characterize the porosity; the densities of the first and second batches were 639 ± 23 and 529 ± 7.9 kg/m³, respectively.

The entire failure process of the second set of specimens was recorded in accordance with the J -integral procedures described earlier. Fig. 18 shows the traction–separation laws that were obtained from this set of specimens at three different loading rates. For the same loading rates, the cohesive strength was smaller than that of the first batch. Fig. 19 shows several representative photographs at progressive stages of deformation for the loading rate of 0.2 mm/s. Fig. 19(a) corresponds to the initial crack prior to loading ①. Several pores along the mating surface are visible. The onset of blunting ② can be seen in Fig. 19(b) as the cohesive stress was increasing and the pores were developing in the cohesive zone. Further blunting can be seen (Fig. 19(c)) accompanied by pore growth. This stage ③ corresponds to the peak cohesive stress. In Fig. 19(d), the crack blunting was severe. The pores grew further in both directions normal and transverse to the load and the pore coalescence started during stage ④ where the cohesive stress was decreasing. The final stage ⑤ of the pore coalescence process corre-

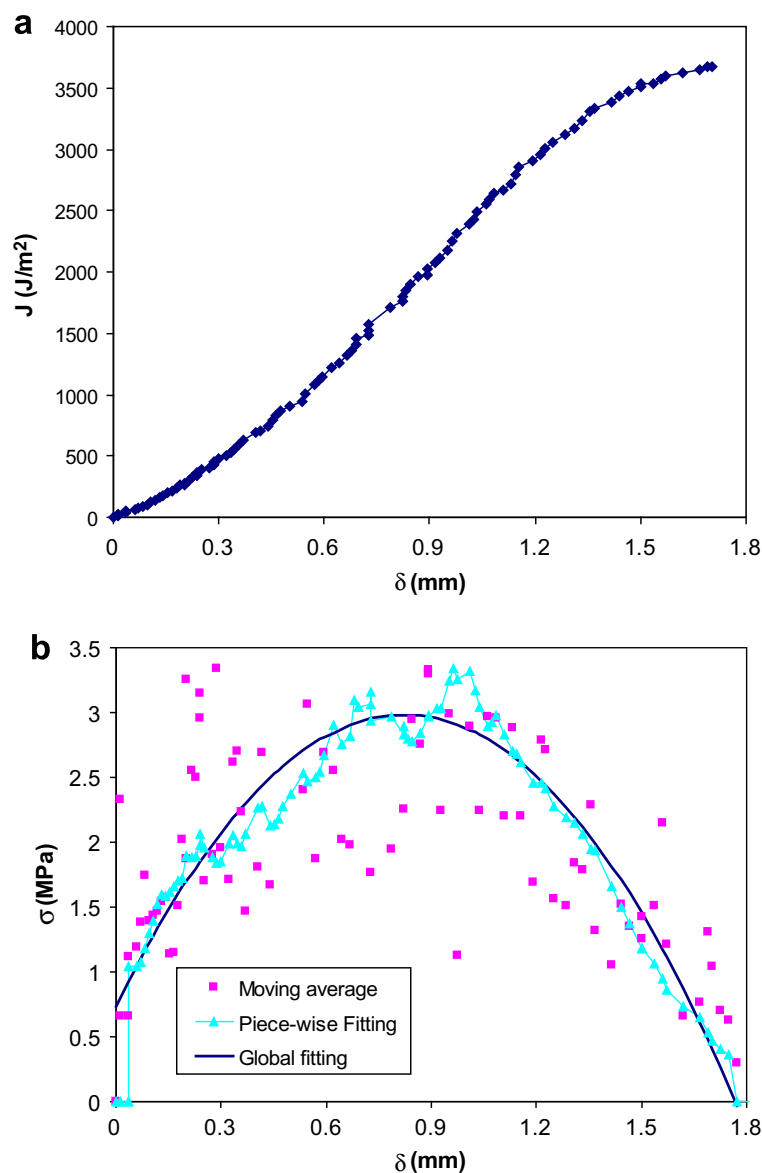


Fig. A1. (a) An example of J - δ curve for a polyurea/steel adhesive joint. (b) The traction–separation laws obtained using three numerical methods for differentiation. δ in both figures is the normal displacement.

sponds to zero cohesive stress and the growth of the interfacial crack, as shown in Fig. 19(e). This failure seems to be a combination of the first and the third mechanisms depending on the stress field ahead of the crack tip and the initial void locations and sizes.

5. Conclusions

Mode 1 and mode 2 traction–separation laws have been obtained for polyurea/steel sandwich specimens. The cohesive laws were obtained directly from experiments by differentiation of simultaneously measured data (the J -integral and the end-opening displacement). Several important observations of the traction–separation laws and the associated interfacial fracture features are summarized in the following.

- (1) The traction–separation laws are highly nonlinear. In fact the mode 1 traction–separation law can be fitted well with a quadratic polynomial.
- (2) Both mode 1 and mode 2 traction–separation laws exhibited pronounced rate dependence. In both cases, the fracture toughness and the peak cohesive stress increased with loading rate, while the critical opening displacement decreased with loading rate.
- (3) Both loading modes gave rise to interfacial debonding near the original cohesive crack-tip.
- (4) The traction–separation laws obtained here represented the behavior of the interphase.
- (5) Another batch of sandwich specimens consisting of polyurea with a higher degree of porosity was tested. The specimens failed by near-tip void growth/coalescence and/or high triaxiality induced cavitation ahead of the crack tip.

Now that we have both mode 1 and mode 2 traction–separation laws, we can incorporate them into mixed-mode cohesive models (Tvergaard and Hutchinson, 1993; Yang and Thouless, 2001) to predict the mixed-mode behavior of structures involving polyurea/steel interfaces at different loading rates. However, it should be borne in mind that the nominal strain rates across the adhesive layer examined in this paper only ranged from 0.003 to 3 s^{-1} . The determination of traction–separation laws at higher loading rates, where inertia effects must be taken into account is currently underway.

Acknowledgements

This work was supported by the Office of Naval Research with Dr. Roshdy Barsoum as program manager. The insightful comments of both reviewers were very helpful in preparing the final version of this paper.

Appendix. The accuracy of the direct approach relies on the numerical differentiation of the J -integral with respect to the end-opening displacement. Moving average, piecewise fitting and global fitting were considered and are briefly described below. Fig. A1(a) shows a typical J integral vs. end-opening displacement response that served as the basis for the examination.

A moving average filter smoothes data by replacing each data point with the average of the neighboring data points defined within a given span. This process is equivalent to low-pass filtering with the response of the smoothing given by the difference equation

$$y_s(i) = \frac{1}{2n+1} [y(i-n) + y(i-n+1) + \dots + y(i+n)],$$

where $y_s(i)$ is the smoothed value for the i th data point, n is the number of neighboring data points on either side of $y(i)$, and $2n+1$ is the span. The end points are not smoothed because a span cannot be defined. After the J -integral data are smoothed, direct differentiation is performed with respect to the end-opening displacement using a central difference scheme.

For piecewise fitting, consider a large number of sets of data for the J -integral and end-opening displacement. For data set number i , a quadratic polynomial is fitted to the data sets ranging from $(i-n)$ to $(i+n)$, where n is as defined above. The slope of the polynomial is the stress corresponding to the i th value of end-opening displacement. Since the first and last several data points cannot be fitted with polynomial equations, stress values for these points are omitted.

The last method to be considered was global fitting. One cubic polynomial equation was able to fit the J - δ data very well. The slope of this polynomial equation yields the stress value for each end opening displacement. This method yielded the most reasonable traction–separation law and was therefore adopted throughout the study.

References

- Arcan, M., Hashin, Z., Voloshin, A., 1978. Method to produce uniform plane-stress states with applications to fiber-reinforced materials. *Experimental Mechanics* 18 (4), 141–146.
- Banks-Sills, L., Sherman, D., 1991. JII fracture testing of a plastically deforming material. *International Journal of Fracture* 50 (1), 15–26.
- Barenblatt, G.I., 1962. The mathematical theory of equilibrium cracks in brittle fracture. *Advances in Applied Mechanics* 7, 55–129.
- Carlsson, L.A., Gillespie, J.W., Pipes, R.B., 1986. On the analysis and design of the end notched flexure (ENF) specimen for mode-I testing. *Journal of Composite Materials* 20 (6), 594–604.

- Chai, H., Chiang, M.Y.M., 1996. A crack propagation criterion based on local shear strain in adhesive bonds subjected to shear. *Journal of the Mechanics and Physics of Solids* 44 (10), 1669–1689.
- Choi, S.H., Song, B.G., Kang, K.J., Fleck, N.A., 2001. Fracture of a ductile layer constrained by stiff substrates. *Fatigue & Fracture of Engineering Materials & Structures* 24 (1), 1–13.
- Cotterell, B., Mai, Y.W., 1996. *Fracture Mechanics of Cementitious Materials*. Blackie, London.
- Cox, B.N., Marshall, D.B., 1991. The determination of crack bridging forces. *International Journal of Fracture* 49 (3), 159–176.
- Dugdale, D.S., 1960. Yielding of steel sheets containing slits. *Journal of the Mechanics and Physics of Solids* 8, 100–104.
- Flinn, B.D., Lo, C.S., Zok, F.W., Evans, A.G., 1993. Fracture-resistance characteristics of a metal-toughened ceramic. *Journal of the American Ceramic Society* 76 (2), 369–375.
- Gu, P., 1995. Notch sensitivity of fiber-reinforced ceramics. *International Journal of Fracture* 70, 253–266.
- Högberg, J.L., Sorensen, B.F., Stigh, U., 2007. Constitutive behaviour of mixed mode loaded adhesive layer. *International Journal of Solids and Structures* 44, 8335–8354.
- Hutchinson, J.W., Suo, Z., 1992. Mixed-mode cracking in layered materials. *Advances in Applied Mechanics* 29, 63–191.
- Ivankovic, A., Pandya, K.C., Williams, J.G., 2004. Crack growth predictions in polyethylene using measured traction–separation curves. *Engineering Fracture Mechanics* 71 (4–6), 657–668.
- Jacobsen, T.K., Sørensen, B.F., 2001. Mode I intra-laminar crack growth in composites – modelling of R-curves from measured bridging laws. *Composites Part A: Applied Science and Manufacturing* 32 (1), 1–11.
- Jin, Z.H., Sun, C.T., 2005. Cohesive fracture model based on necking. *International Journal of Fracture* 134 (2), 91–108.
- Kim, K.S., Aravas, N., 1988. Elastoplastic analysis of the peel test. *International Journal of Solids and Structures* 24, 417–435.
- Kinloch, A.J., Lau, C.C., Williams, J.G., 1994. The peeling of flexible laminates. *International Journal of Fracture* 66, 45–70.
- Landis, C.M., Pardo, T., Hutchinson, J.W., 2000. Crack velocity dependent toughness in rate dependent materials. *Mechanics of Materials* 32 (11), 663–678.
- Leffler, K., Alfredsson, K.S., Stigh, U., 2007. Shear behaviour of adhesive layers. *International Journal of Solids and Structures* 44, 530–545.
- Liechti, K.M., Knauss, W.G., 1982. Crack-propagation at material interfaces. 2. Experiments on mode interaction. *Experimental Mechanics* 22 (10), 383–391.
- Liechti, K.M., Wu, J.D., 2001. Mixed-mode, time-dependent rubber/metal debonding. *Journal of the Mechanics and Physics of Solids* 49 (5), 1039–1072.
- Li, V.C., Chan, C.-M., Leung, C.K.Y., 1987. Experimental determination of the tension-softening relations for cementitious composites. *Cement and Concrete Research* 17, 441–452.
- Li, S., Thouless, M.D., Waas, A.M., Schroeder, J.A., Zavattieri, P.D., 2005a. Use of a cohesive-zone model to analyze the fracture of a fiber-reinforced polymer–matrix composite. *Composites Science and Technology* 65 (3–4), 537–549.
- Li, S., Thouless, M.D., Waas, A.M., Schroeder, J.A., Zavattieri, P.D., 2005b. Use of mode-I cohesive-zone models to describe the fracture of an adhesively-bonded polymer–matrix composite. *Composites Science and Technology* 65 (2), 281–293.
- Li, S., Thouless, M.D., Waas, A.M., Schroeder, J.A., Zavattieri, P.D., 2006. Mixed-mode cohesive-zone models for fracture of an adhesively bonded polymer–matrix composite. *Engineering Fracture Mechanics* 73 (1), 64–78.
- Massabo, R., Mumm, D.R., Cox, B.N., 1998. Characterizing mode II delamination cracks in stitched composites. *International Journal of Fracture* 92 (1), 1–38.
- Mello, A.V., Liechti, K.M., 2006. The effect of self-assembled monolayers on interfacial fracture. *Journal of Applied Mechanics* 73, 860–870.
- Mohammed, I., Liechti, K.M., 2000. Cohesive zone modeling of crack nucleation at bimaterial corners. *Journal of the Mechanics and Physics of Solids* 48 (4), 735–764.
- Needleman, A., 1987. A continuum model for void nucleation by inclusion debonding. *Journal of Applied Mechanics-Transactions of the Asme* 54 (3), 525–531.
- Needleman, A., 1990. An analysis of tensile decohesion along an interface. *Journal of the Mechanics and Physics of Solids* 38 (3), 289–324.
- Pandya, K.C., Williams, J.G., 2000. Measurement of cohesive zone parameters in tough polyethylene. *Polymer Engineering and Science* 40 (8), 1765–1776.
- Parmigiani, J.P., Thouless, M.D., 2007. The effects of cohesive strength and toughness on mixed-mode delamination of beam-like geometries. *Engineering Fracture Mechanics* 74, 2675–2699.
- Popelar, C.F., Liechti, K.M., 1997. Multiaxial nonlinear viscoelastic characterization and modeling of a structural adhesive. *Journal of Engineering Materials and Technology-Transactions of the Asme* 119 (3), 205–210.
- Popelar, C.F., Liechti, K.M., 2003. A distortion-modified free volume theory for nonlinear viscoelastic behavior. *Mechanics of Time-Dependent Materials* 7 (2), 89–141.
- Shih, C.F., Asaro, R.J., O'Dowd, N.P., 1991. Elastic–plastic analysis of cracks on bimaterial interfaces. 3. Large-scale yielding. *Journal of Applied Mechanics* 58 (2), 450–463.
- Shirani, A., Liechti, K.M., 1998. A calibrated fracture process zone model for thin film blistering. *International Journal of Fracture* 93 (1–4), 281–314.
- Sorensen, B.F., 2002. Cohesive law and notch sensitivity of adhesive joints. *Acta Materialia* 50 (5), 1053–1061.
- Sorensen, B.F., Jacobsen, T.K., 2003. Determination of cohesive laws by the J integral approach. *Engineering Fracture Mechanics* 70 (14), 1841–1858.
- Swadener, J.G., Liechti, K.M., 1998. Asymmetric shielding mechanisms in the mixed-mode fracture of a glass/epoxy interface. *Journal of Applied Mechanics* 65 (1), 25–29.
- Takas, T.P., 2004. 100% solids aliphatic polyurea coatings for direct-metal applications. *JCT Coatingstech* 1 (5), 40–45.
- Tvergaard, V., Hutchinson, J.W., 1993. The influence of plasticity on mixed-mode interface toughness. *Journal of the Mechanics and Physics of Solids* 41 (6), 1119–1135.
- Tvergaard, V., Hutchinson, J.W., 1994. Toughness of an interface along a thin ductile layer joining elastic solids. *Philosophical Magazine a-Physics of Condensed Matter Structure Defects and Mechanical Properties* 70 (4), 641–656.
- Varias, A.G., Suo, Z., Shih, C.F., 1991. Ductile failure of a constrained metal foil. *Journal of the Mechanics and Physics of Solids* 39 (7), 963–986.
- Wang, S.S., 1983. Fracture-mechanics for delamination problems in composite-materials. *Journal of Composite Materials* 17 (3), 210–223.
- Wei, Y., Hutchinson, J.W., 1998. Interface strength, work of adhesion and plasticity in the peel test. *International Journal of Fracture* 93 (1–4), 315–333.
- Yang, Q.D., Thouless, M.D., 2001. Mixed-mode fracture analyses of plastically-deforming adhesive joints. *International Journal of Fracture* 110 (2), 175–187.
- Yang, Q.D., Thouless, M.D., Ward, S.M., 2000. Analysis of the symmetrical 90 degrees-peel test with extensive plastic deformation. *Journal of Adhesion* 72 (2), 115.